doi: 10.34248/bsengineering.1759120



Research Article

Volume 8 - Issue 5: 1585-1594 / September 2025

NUMERICAL INVESTIGATION OF HYDROFOIL CAVITATION USING OPENFOAM: EFFECT OF THICKNESS AND CAMBER

Mehmet Numan KAYA1*

¹Necmettin Erbakan University, Faculty of Engineering, Department of Mechanical Engineering, Konya, Türkiye

Abstract: Cavitation is a critical phenomenon in hydrodynamic applications, significantly influencing the performance and durability of hydrofoils. This study presents a numerical investigation of cavitation over hydrofoils, focusing on the effects of thickness and camber, using the interPhaseChangeFoam solver within the OpenFOAM framework. The numerical setup was validated against experimental data for the NACA66(mod) hydrofoil. Simulations were performed at a fixed angle of attack of 4° under two cavitation numbers, $\sigma = 0.84$ and $\sigma = 0.91$ using the Schnerr-Sauer cavitation model with a vapor pressure of 2420 Pa. To assess thickness effects, symmetric hydrofoils NACA0012, NACA0016, and NACA0020 were analyzed, while camber effects were examined using hydrofoils of identical thickness but varying camber, NACA0012, NACA2412, and NACA4412. Results show that cambered and thicker hydrofoils develop more extensive cavitation regions. Increasing the cavitation number generally leads to higher lift coefficients, with the effect more pronounced for cambered profiles. Greater camber promotes earlier cavitation inception, a larger cavity extent, and higher lift, with NACA4412 achieving the highest lift coefficients of approximately $C_L = 0.74$ and 0.79 at $\sigma = 0.84$ and 0.91, respectively. Increased thickness also enlarges the cavitation region but generally results in lower lift, as observed for NACA0020, which exhibited lift coefficients of approximately $C_L = 0.31$ and 0.34 at $\sigma = 0.84$ and 0.91, respectively. Increasing the cavitation number from $\sigma = 0.84$ to 0.91 reduced drag for all profiles by up to about 23% while preserving lift in cambered foils.

Keywords: Cavitation, Hydrofoil, Thickness, Camber, CFD, OpenFOAM

*Corresponding author: Necmettin Erbakan University, Faculty of Engineering, Department of Mechanical Engineering, Konya, Türkiye E mail: mnkaya@erbakan.edu.tr (M.N. KAYA)

https://orcid.org/0000-0003-3116-9442 Mehmet Numan KAYA

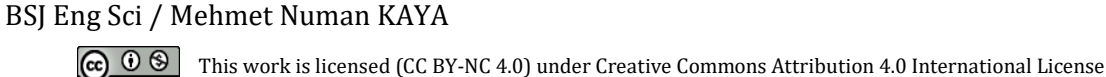
Received: August 05, 2025 Accepted: September 09, 2025 Published: September 15, 2025

Cite as: Kaya MN. 2025. Numerical investigation of hydrofoil cavitation using openfoam: Effect of thickness and camber. BSJ Eng Sci, 8(5): 1585-1594.

1. Introduction

Cavitation, the rapid phase change from liquid to vapor when local pressure drops below the vapor-pressure threshold, remains one of the most critical, and still incompletely understood, phenomena in the hydrodynamic performance and durability of lifting surfaces such as hydrofoils (Adil et al., 2025). In practical applications, cavitation can trigger drastic lift/drag fluctuations, high-amplitude pressure pulses, broadband noise, and material erosion, thereby limiting operating envelopes and shortening service life (Qiu et al., 2025). As performance targets tighten and design margins shrink, a predictive, physics-based understanding of cavitation on hydrofoils has become indispensable.

Numerical investigations have systematically examined how multiple physical and operating parameters govern cavitation on hydrofoils. Early investigations by Kang et al. (2014) showed, for a Clark-Y profile, that both cavity length and lift/drag increase monotonically with angle of attack over several cavitation numbers. Karim et al. (2018) carried out finite-volume RANS calculations on NACA 0012/0021 foils, independently sweeping cavitation number (σ) and angle of attack (α), and their results showed that cavity length and lift-drag trends are more sensitive to α at fixed $\sigma.$ Guo et al. (2023) extended parameter studies through a combined experimental/CFD effort with viscous oil, varying velocity, pressure, temperature, and α , revealing that pressure had the strongest influence on vapor-volume growth while temperature effects were secondary. The interaction of cavitation with flow dynamics has been shown to be crucial for understanding hydrofoil performance. The nucleation and dynamics of cavitation bubbles have been investigated by Huang et al. (2014), who revealed that bubble formation and interaction with hydrofoil surfaces can lead to material degradation, erosion, and performance loss, with flow conditions directly influencing cavitation erosion intensity. Peng et al. (2016) demonstrated the effectiveness combining of experimental observations with numerical simulations in advancing cavitation understanding, providing critical insights into cloud cavitation and its associated flow structures while validating numerical model reliability. Recently, Chen and Escaler (2024) conducted numerical investigations of cavitation effects on wake dynamics behind a blunt trailing edge NACA 0009 hydrofoil, finding that cavitation development enhances vortex shedding frequency while decreasing streamwise inter-vortex spacing, with substantial increases in both lift (C_L) and drag (C_D) coefficients observed as vortex cavitation size



grows. Kumar et al. (2024) introduced passive geometric controls, a rectangular pimple and finite trailing edge, on a cambered NACA 4412 and demonstrated that the pimple suppressed cloud shedding and postponed the onset of supercavitation relative to the baseline foil. Usta et al. (2025) performed numerical simulations to investigate the effects of leading-edge tubercles and surface corrugations on twisted hydrofoils, finding that tubercles delayed stall and reduced cavitation formation. Gallegos and Luo (2024) performed a 3-D RANS study of a circularleading-edge hydrofoil in which σ , Reynolds number, and three turbulence closures were systematically varied. They concluded that the MSST-PANS model best reproduced the cloud-cavitation regime and its shedding frequency. Mostafa et al. (2016) adopted a bubbledynamics cavitation model and compared three RANS turbulence closures across multiple σ - α combinations. finding that the SST $k-\omega$ scheme captured unsteady sheetto-cloud transitions most faithfully. Wang et al. (2025) coupled an implicit LES with the Schnerr-Sauer model to probe how an upstream cylinder wake, together with changes in σ and α , modifies vortex-induced pressure fluctuations on a downstream hydrofoil, highlighting the pivotal role of wake shedding frequency in cloudcavitation dynamics.

Collectively, these studies underscore that cavitation behaviour is highly multi-parametric: turbulence modelling, cavitation number, Reynolds number, inflow unsteadiness, geometric modifications including thickness and camber variations all interact to dictate inception thresholds, cavity topology, and associated hydrodynamic loads. Despite these comprehensive investigations, the individual and isolated effects of thickness and camber on cavitation characteristics remain insufficiently explored. The present study addresses this gap by conducting a systematic numerical investigation using OpenFOAM's interPhaseChangeFoam solver with the Schnerr-Sauer cavitation model to examine the individual contributions of thickness and camber variations on cavitation, thereby offering fundamental, parameter-isolated understanding of the role of thickness and camber in governing cavitation behaviour, which can directly support both theoretical modelling and practical hydrofoil design.

2. Materials and Methods

2.1. Numerical Approach

Computational Fluid Dynamics (CFD) was employed to simulate cavitating flow over hydrofoils using the open-source OpenFOAM framework. The governing equations 1 and 2 are based on the finite volume discretization of the incompressible Reynolds-Averaged Navier–Stokes (RANS) equations, coupled with a volume-of-fluid (VOF) formulation to capture the liquid-vapor interface. The equations of mass and momentum conservation are expressed as (Canlı et al., 2020; Kaya et al., 2025; Manolesos et al., 2024; Zhou and Wang, 2008):

$$\frac{\partial \rho}{\partial t} + \nabla \cdot (\mathbf{V}\rho) = 0 \tag{1}$$

$$\frac{\partial(\rho \mathbf{V})}{\partial t} + \nabla \cdot (\rho \mathbf{V} \mathbf{V}) = -\nabla p + \nabla(\mu \nabla \mathbf{V}) + \rho \mathbf{g}$$
 (2)

where ρ is the local density depending on vapor volume fraction, **V** is the velocity vector, p is pressure, μ is dynamic viscosity, and g is gravitational acceleration. The turbulence was modeled using the standard k- ϵ model, governed by the following transport equations 3 and 4 for turbulent kinetic energy (k) and turbulent dissipation (ϵ) :

$$\frac{\partial(\rho k)}{\partial t} + \nabla \cdot (\rho \mathbf{V} k) = \nabla \cdot \left[\left(\mu + \frac{\mu_t}{\sigma_k} \right) \nabla k \right] + P_k - \rho \varepsilon \tag{3}$$

$$\frac{\partial(\rho\varepsilon)}{\partial t} + \nabla \cdot (\rho \mathbf{V}\varepsilon) = \nabla \cdot \left[\left(\mu + \frac{\mu_t}{\sigma_{\varepsilon}} \right) \nabla \varepsilon \right] + C_{\{1\varepsilon\}} \left(\frac{\varepsilon}{k} \right) P_k - C_{\{2\varepsilon\}} \rho \left(\frac{\varepsilon^2}{k} \right)$$
(4)

where P_k is the production of turbulent kinetic energy, and μ_t is the eddy viscosity. The standard k– ε turbulence model was selected for its reliability in cavitating flow simulations and its ability to provide stable, accurate results without the need for excessive near-wall refinement. The model also produced results in good agreement with experimental validation data, as presented in section 2.4. In this study, y^+ values were maintained within the range of approximately 30–100, which is consistent with the recommended range for this turbulence model.

2.2. Cavitation Modelling

Cavitation was simulated using the interPhaseChangeFoam solver in OpenFOAM, which solves the incompressible two-phase flow using the VOF method with mass transfer between liquid and vapor phases. The Schnerr–Sauer cavitation model was adopted to model the phase change process (Schnerr and Sauer, 2001). The mass transfer source term in the continuity equation is defined based on bubble dynamics as (Arndt, 2012; Kubota et al., 1992):

$$\dot{\mathbf{m}} = C_v \cdot \frac{3\alpha_l (1 - \alpha_l)\rho_l}{R_b} \sqrt{\left[\frac{2}{3} \cdot \frac{p_v - p}{\rho_l}\right]} , if \ p < p_v$$
 (5)

$$\dot{\mathbf{m}} = C_c \cdot \frac{3\alpha_v (1 - \alpha_v)\rho_v}{R_b} \sqrt{\left[\frac{2}{3} \cdot \frac{p - p_v}{\rho_l}\right]}, if \ p > p_v \qquad (6)$$

where vapor pressure of water is p_v =2420, bubble diameter is $R_b = 2 \times 10^{-6} \, \text{m}$, α_l and α_v are liquid and vapor volume fractions, evaporation and condensation coefficients are C_v =1 and $C_c = 1$, ρ_l and ρ_v are liquid and vapor densities. equation 5 represents the evaporation process, activated when the local pressure p is below p_v , while equation 6 models condensation, occurring when p exceeds p_v . The cavitation number is calculated as (equation 7):

$$\sigma = \frac{p_{\infty} - p_{\nu}}{0.5 \cdot \rho \cdot U^2} \tag{7}$$

where σ =0.84 and 0.91 were selected to represent moderate and weak cavitation regimes, respectively.

Time-dependent simulations were run over 20 seconds of physical time, and the last 5 seconds were used to average liftand drag coefficients, ensuring steady-state behavior and statistical convergence. The simulation setup, including boundary conditions, mesh parameters, and solver settings, was chosen to ensure a balance between numerical accuracy and computational efficiency,

providing a reproducible framework for similar cavitation studies. BaramFlow was used as the graphical user interface for OpenFOAM simulations.

2.3. Tested Hydrofoils

To investigate the effects of geometric parameters on cavitation behavior, two separate hydrofoil groups were analyzed: one focusing on thickness and the other on camber.

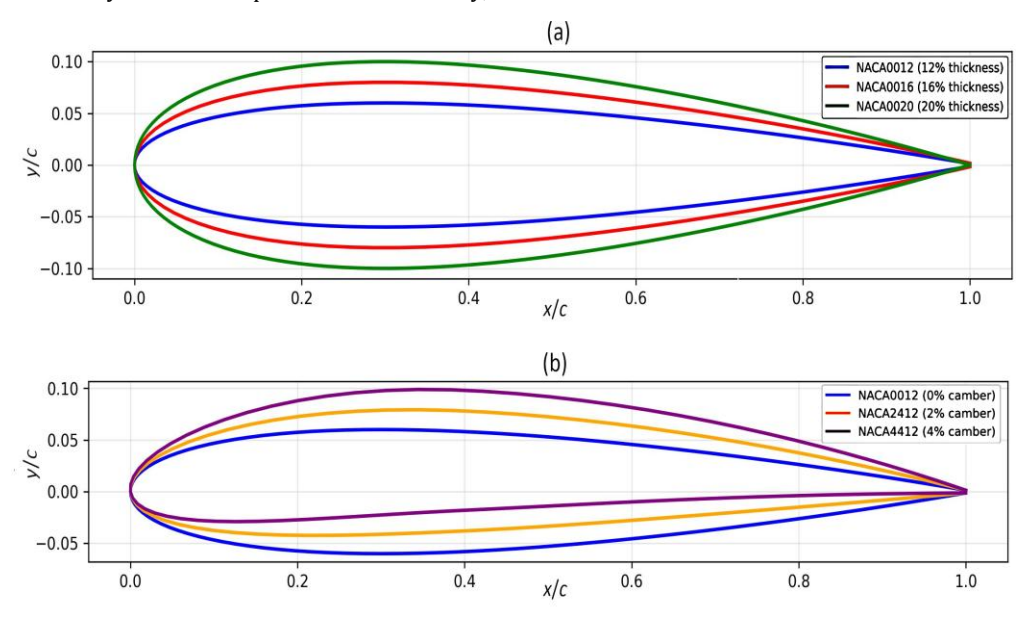


Figure 1. Hydrofoil geometries used in the simulations: (a) NACA0012, NACA0016, NACA0020 (b) NACA0012, NACA2412, NACA4412.

For the thickness effect, symmetric NACA hydrofoils, NACA 0012, NACA 0016, and NACA 0020 were selected, with maximum thicknesses of 12%, 16%, and 20% of the chord, respectively, and zero camber. To examine the effect of camber, three hydrofoils with identical thickness (12%) but varying camber values were studied: NACA 0012 (symmetric), NACA 2412 (2% camber), and NACA 4412 (4% camber). All hydrofoils have the same chord length and were simulated under the same operating conditions to enable a consistent comparison. Geometries of the hydrofoils are presented in Fig. 1.

2.4. Mesh Independence and validation

Three mesh resolutions were generated: coarse, medium, and fine, with 72380, 103148, and 162162 cells, respectively. The numerical results from all three meshes, together with the experimental data (Kim et al., 2010; Shen and Dimotakis, 1989), are compared in Figure 2.

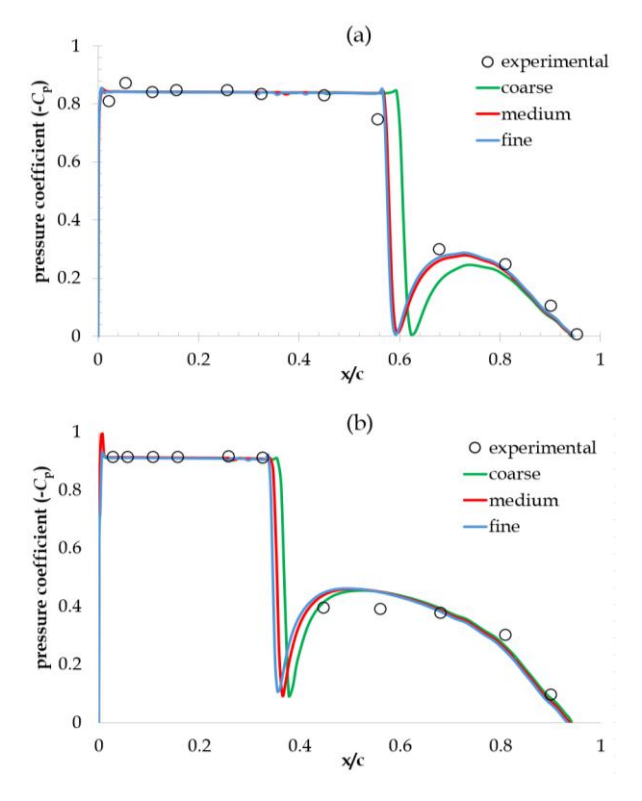


Figure 2. Mesh independence study and validation based on pressure coefficient (C_p) distribution over the NACA66(mod) hydrofoil at an angle of attack of 4° for (a) $\sigma = 0.84$ (b) $\sigma = 0.91$.

For $\sigma=0.84$ (Figure 2a), the onset of the pressure drop occurs at approximately $x/c\approx0.60$ for the fine and medium meshes, while the coarse mesh shows a slight delay of about $\Delta x/c\approx0.02$. For $\sigma=0.91$ (Figure 2b), the pressure drop begins earlier at around $x/c\approx0.38$ for all meshes, with the coarse mesh exhibiting a marginal delay of less than $\Delta x/c\approx0.01$. These results confirm that the medium mesh provides mesh-independent performance while ensuring computational efficiency; therefore, it was

selected for further analysis. Images of the selected medium mesh are presented in Figure 3. All simulations were performed with a Courant number (CFL) of 1. Validation was carried out using the NACA66(mod) hydrofoil at a 4° angle of attack under both cavitation numbers, showing strong agreement in both pressure distribution and cavity extent, confirming the reliability of the numerical setup.

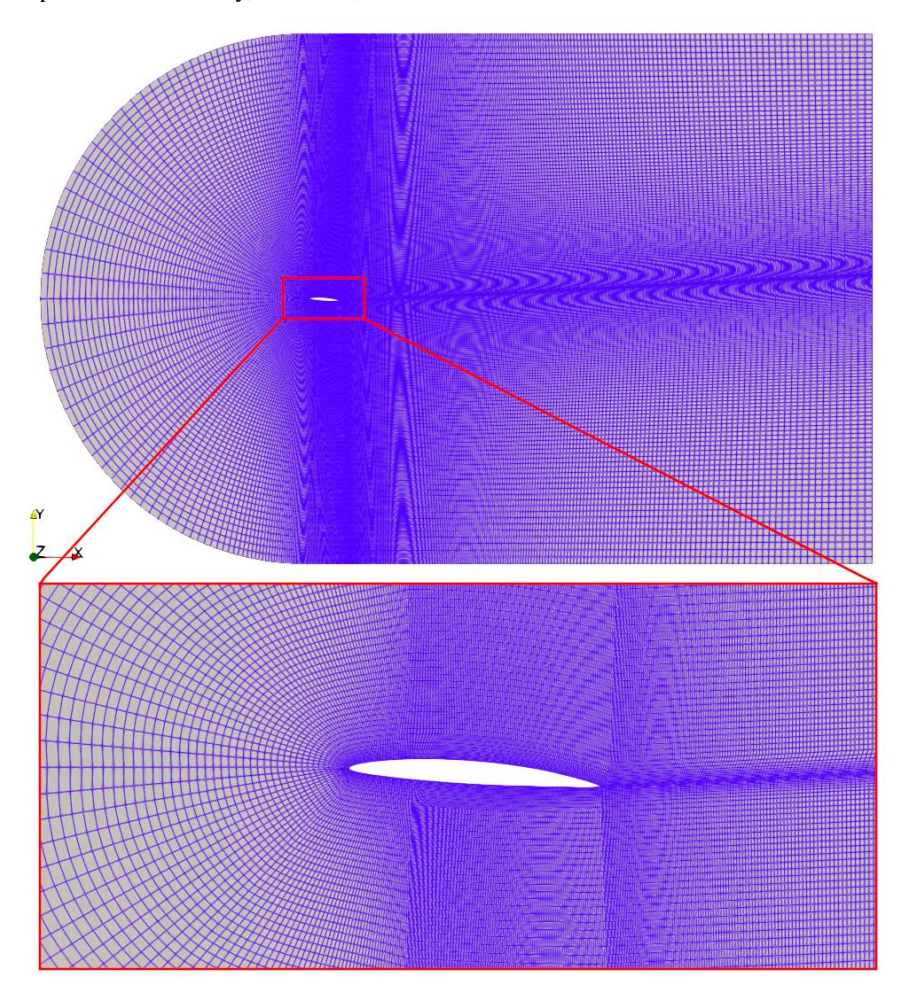


Figure 3. Medium-resolution computational grid selected for further analysis. The illustration shows the overall computational domain (top) and a zoomed-in view around the hydrofoil (bottom).

3. Results and Discussion

This section presents the cavitation characteristics obtained from unsteady simulations performed using the interPhaseChangeFoam solver. The spatial evolution of cavitation structures over the hydrofoil surface for each geometry was analyzed for cavitation number $\sigma{=}0.84,$ captured at four nondimensional time instances: $t^*=0.1,$ 0.4, 0.7, and 1.0 and presented in Figure 4. The time-dependent development of cavitation is illustrated through contours of the liquid water volume fraction (α_{water}) at selected nondimensionalized time instances. Time normalization was carried out using a reference time of $t_R=10$ seconds, i.e., $t/t_R{=}\ t^*.$

The cavitation development over time differs significantly between symmetric and cambered airfoils. In general, cavitation begins near the leading edge and gradually extends downstream with time. The cambered profiles, NACA2412 and NACA4412, exhibit stronger and more pronounced cavitation clouds, especially during the midto-late stages ($t/t_R = 0.4-1.0$). In addition, increase in camber caused to extension of cavitation clouds. In contrast, symmetric airfoils such as NACA0012, NACA0016, and NACA0020 tend to show more localized and stable cavitation patterns. The thickness of the airfoil also increases the extent of cavitation, as observed in the increasing coverage from NACA0012 to NACA0020. Moreover, the asymmetric profiles demonstrate earlier cavitation inception and a broader cavity region due to their higher suction peak near the leading edge. Figure 5 presents the distribution of the liquid water volume fraction on the hydrofoil surfaces for two different cavitation numbers.

The top two rows correspond to the more aggressive cavitating condition at σ = 0.84 while the bottom two rows show results for a milder condition at σ =0.91. The comparison highlights the role of cavitation number in

determining cavity extent and shape. As expected, lower σ results in more developed vapor regions and longer attached cavity structures, particularly for thicker or cambered hydrofoils.

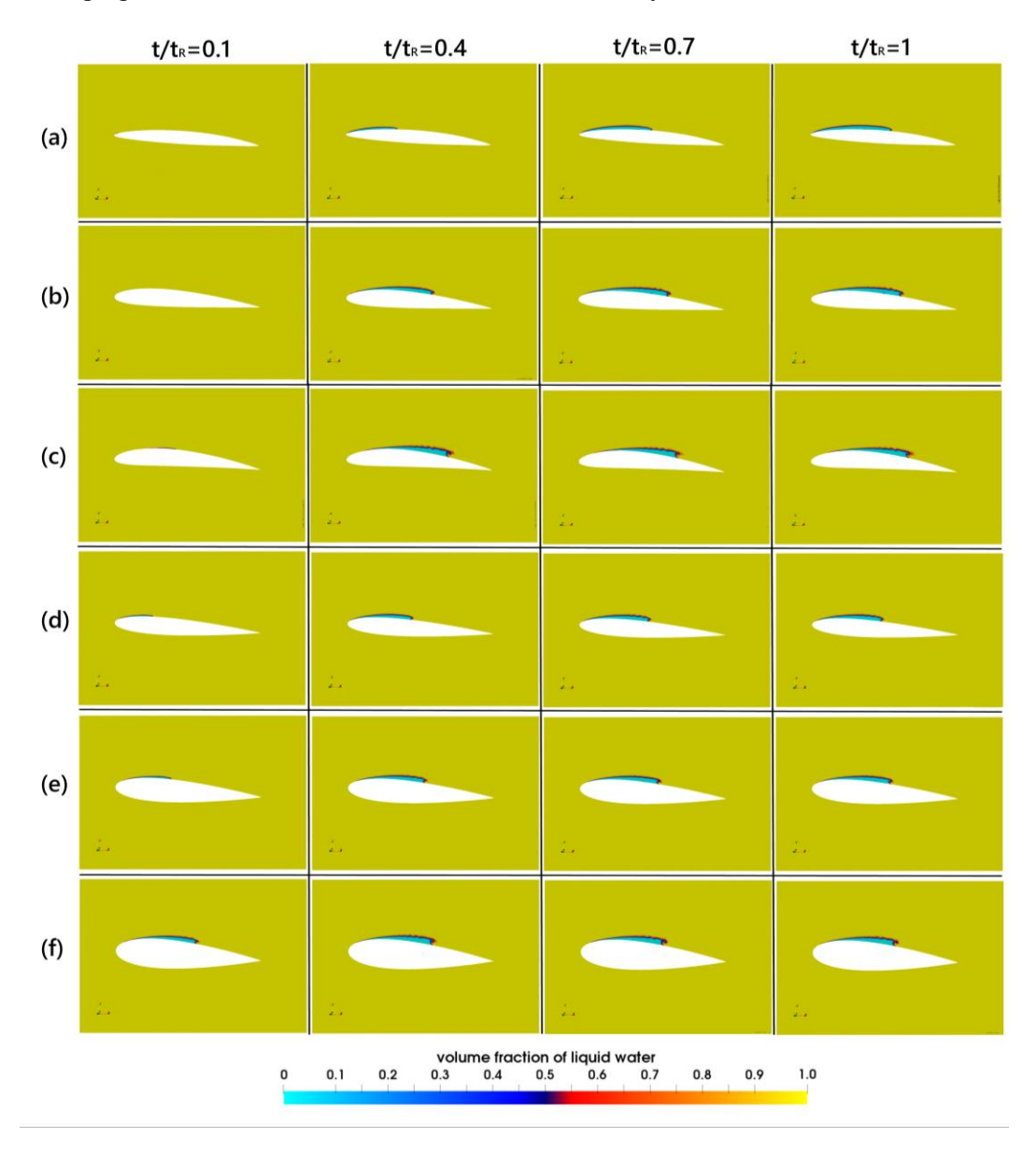


Figure 4. Time evolution of cavitation structures for different airfoils at a cavitation number of σ = 0.84. From top to bottom: (a) NACA66, (b) NACA2412, (c) NACA4412, (d) NACA0012, (e) NACA0016, and (f) NACA0020. The snapshots correspond to nondimensional time instances t/t_R = 0.1, 0.4, 0.7, and 1.0 from left to right. Color contours represent the volume fraction of liquid water.

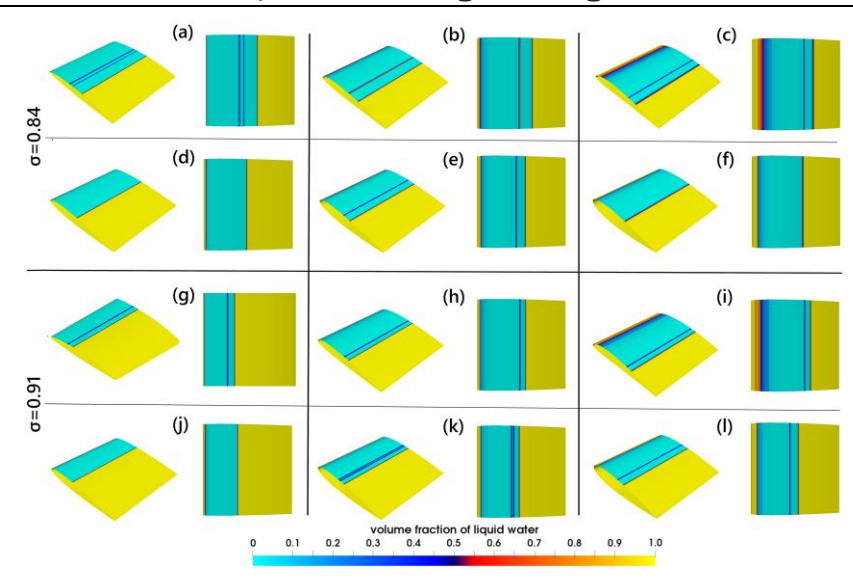


Figure 5. Distribution of liquid water volume fraction over various hydrofoils at two cavitation numbers. The top two rows, (a,b,c,d,e,f), correspond to σ = 0.84, and the bottom two rows, (g,h,i,j,k,l), correspond to σ = 0.91. The hydrofoils are (a,g) NACA66, (b,h) NACA2412, (c,i) NACA4412, (d,j) NACA0012, (e,k) NACA0016, and (f,l) NACA0020.

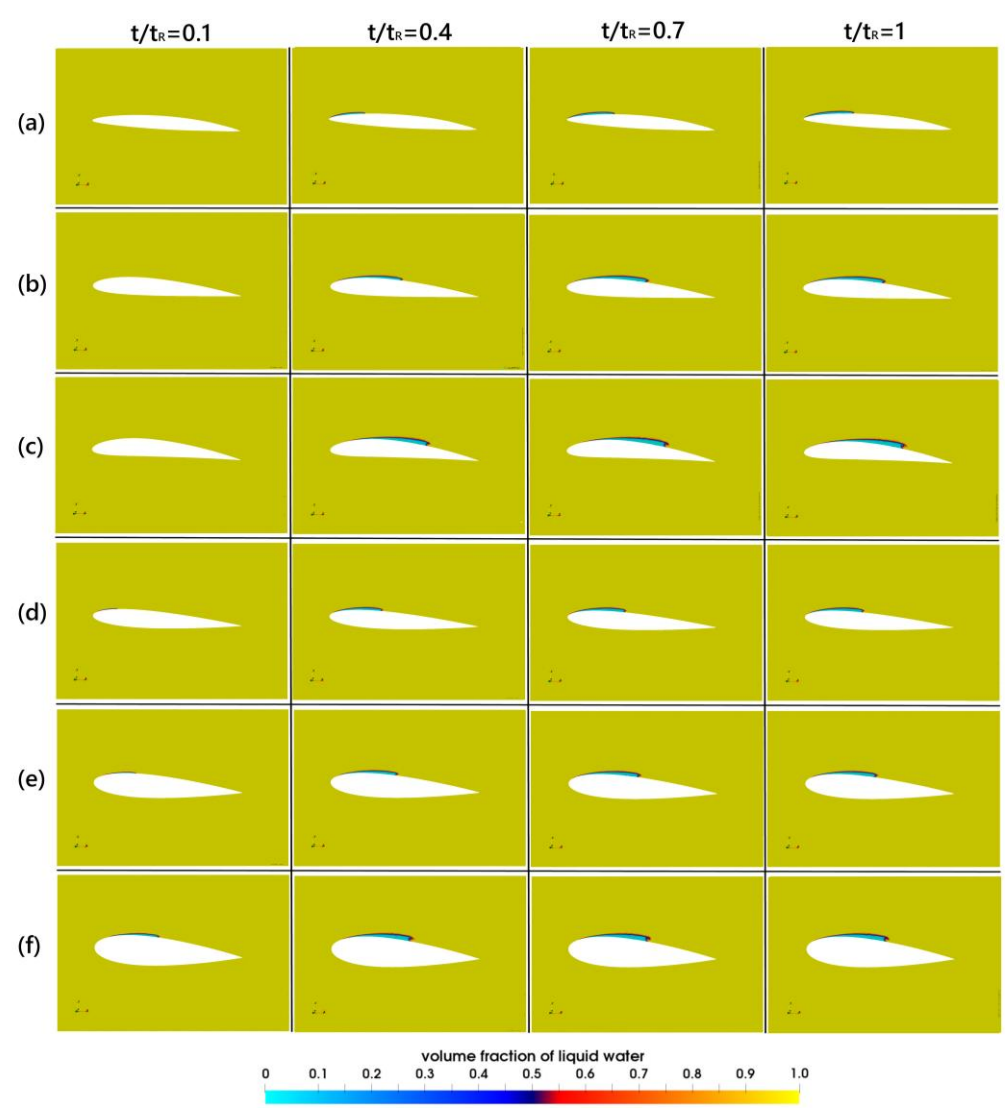


Figure 6. Time evolution of cavitation structures for different airfoils at a cavitation number of σ = 0.91. From top to bottom: (a) NACA66, (b) NACA2412, (c) NACA4412, (d) NACA0012, (e) NACA0016, and (f) NACA0020. The snapshots correspond to nondimensional time instances t/t_R = 0.1, 0.4, 0.7, and 1.0 from left to right. Color contours represent the volume fraction of liquid water.

To further examine unsteady effects, Figure 6 displays the time-dependent cavitation development for σ = 0.91 at the same nondimensional time instants as in Figure 4. Although cavitation is less pronounced than at σ = 0.84, unsteady cavity dynamics are still evident, especially for thicker and cambered profiles. These results support the conclusion that both thickness and camber significantly influence cavitation inception and evolution.

To evaluate the influence of airfoil geometry on cavitation inception and development, pressure coefficient (C_{p}) contours were analyzed at two different cavitation numbers $\sigma=0.84$ and 0.91. As shown in Figure 7 at $\sigma=0.84$, strong low-pressure zones emerge on cambered hydrofoils, especially near the leading edge, due to enhanced suction effects. This pressure drop increases the risk of cavitation formation. The symmetric profiles exhibit relatively moderate pressure drops.

When the cavitation number is increased to σ = 0.91, as seen in Figure 8 the pressure minima weaken across all profiles, which correlates with delayed cavitation onset and less severe cavity formation. Figure 9 visualizes the surface distribution of pressure coefficient over the hydrofoil surfaces. The upper two rows show results for σ = 0.84, and the lower two rows for σ = 0.91. The color gradients indicate the spatial variation of local pressure, and distinct patterns are visible between cambered and symmetric foils. Cambered foils such as NACA66(mod) and NACA4412 exhibit sharper and more extensive low-pressure zones, which are potential sites for cavitation inception.

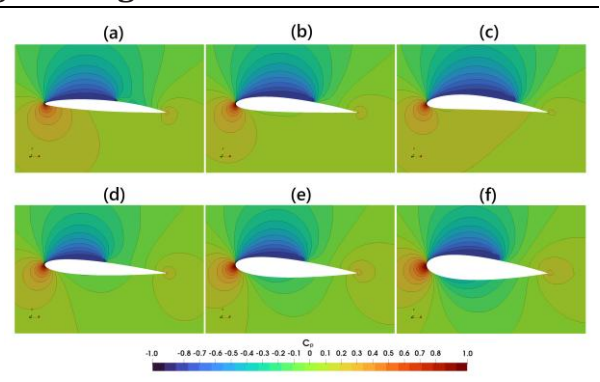


Figure 7. Pressure coefficient (C_p) contours σ =0.84 for (a) NACA66(mod), (b) NACA2412, (c) NACA4412, (d) NACA0012, (e) NACA0016, and (f) NACA0020.

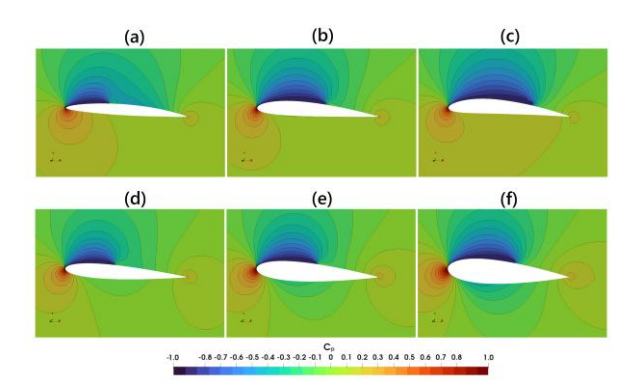


Figure 8. Pressure coefficient (C_p) contours σ =0.91 for (a) NACA66(mod), (b) NACA2412, (c) NACA4412, (d) NACA0012, (e) NACA0016, and (f) NACA0020.

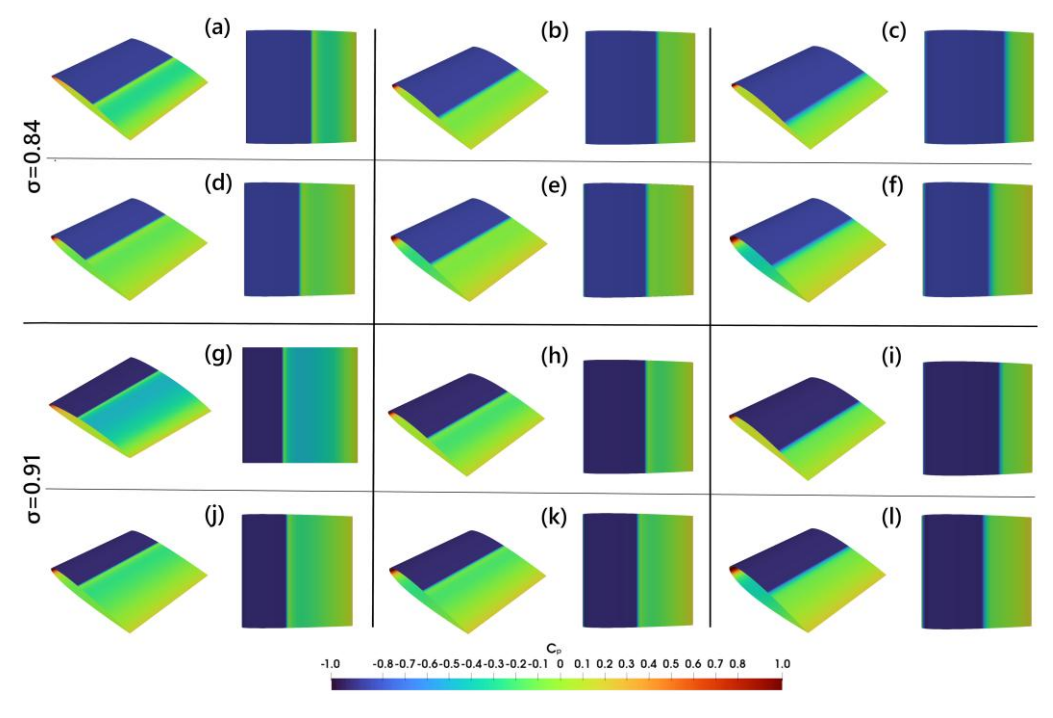


Figure 9. Surface pressure coefficient distributions for all hydrofoils. The upper two rows correspond to σ = 0.84, and the bottom two rows to σ = 0.91. Each two shows (a, g) NACA66(mod), (b, h) NACA2412, (c, i) NACA4412, (d, j) NACA0012, (e, k) NACA0016, and (f, l) NACA0020.

The pressure coefficient distributions presented in Figure 10 demonstrate the significant influence of airfoil geometry parameters on cavitation behavior under different flow conditions. For symmetric airfoils (NACA0012, NACA0016, NACA0020), the thickness effect becomes evident as thicker profiles exhibit more extensive low-pressure regions and susceptibility to cavitation, particularly at higher cavitation numbers. At $\sigma = 0.84$, all symmetric profiles show similar cavitation inception patterns around x/c =0.5, while the NACA0012 demonstrates the most pronounced pressure recovery compared to the thicker NACA0016 and NACA0020 profiles. This thicknessdependent behavior intensifies at σ = 0.91, where the NACA0020 profile maintains the most extensive lowpressure zone, confirming that increased thickness ratio promotes cavitation development. The camber effect analysis reveals equally significant influences on cavitation characteristics, where cambered airfoils (NACA2412, NACA4412) exhibit distinctly different pressure distributions compared to the symmetric NACA0012. The highly cambered NACA4412 profile consistently maintains lower pressure coefficients over broader chord ranges at both cavitation numbers, indicating enhanced cavitation inception likelihood and extended cavitation regions on the suction side. The comparison between $\sigma = 0.84$ and $\sigma = 0.91$ conditions reveals that higher cavitation numbers lead to more extensive cavitation regions and deeper pressure drops across all airfoil geometries, confirming the fundamental relationship between cavitation number and cavitation intensity in hydrofoil applications.

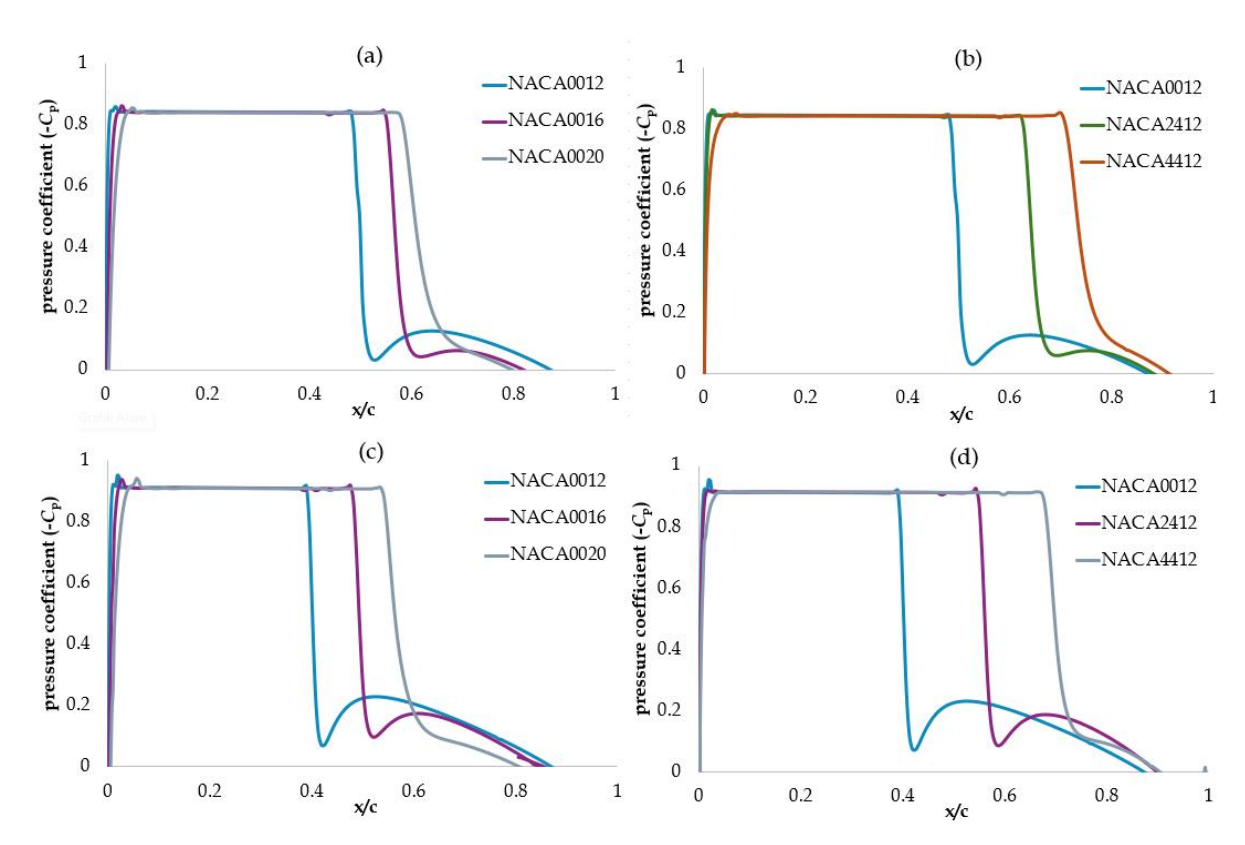


Figure 10. Pressure coefficient distributions on the suction surfaces of hydrofoils at (a,b) σ = 0.84 and (c,d) σ = 0.91.

Table 1 compares the lift and drag coefficients of different hydrofoils under two cavitation conditions. At σ =0.84, cambered hydrofoils like NACA4412 and NACA66 exhibit higher lift coefficients compared to symmetric ones. The drag increases with increasing thickness and camber. When the cavitation number increases to 0.91, the overall drag decreases for all airfoils, while the lift generally remains stable or increases slightly for cambered profiles. This indicates that cavitation has a notable influence on aerodynamic performance, particularly for thin or symmetric hydrofoils.

Table 1. Lift and drag coefficients of the hydrofoils at cavitation numbers $\sigma = 0.84$ and $\sigma = 0.91$

Hydrofoil	$\sigma = 0.84$		$\sigma = 0.91$	
Hydrolon	$C_{\rm L}$	C_{D}	$\mathcal{C}_{ ext{L}}$	\mathcal{C}_{D}
NACA66	0.698	0.019	0.640	0.016
NACA2412	0.617	0.030	0.624	0.023
NACA4412	0.743	0.039	0.792	0.033
NACA0012	0.423	0.025	0.413	0.020
NACA0016	0.376	0.029	0.385	0.023
NACA0020	0.313	0.039	0.343	0.032

5. Conclusions

This study numerically investigates the cavitation behavior of hydrofoils with varying camber and thickness using the interPhaseChangeFoam solver of OpenFOAM. Two cavitation numbers, $\sigma = 0.84$ and 0.91, were considered under a fixed angle of attack of 4°. Timedependent simulations were performed to assess the influence of geometrical parameters on cavitation dynamics. The results show that both camber and thickness significantly affect cavitation development. Cambered hydrofoils generate higher lift and exhibit earlier onset and wider extent of cavitation compared to symmetric profiles. Increasing thickness tends to delay cavitation inception but leads to more pronounced sheet cavitation. For example, the NACA4412 achieved lift coefficients of approximately $C_L = 0.74$ and 0.79 at $\sigma = 0.84$ and 0.91, while the thick symmetric NACA0020 yielded the lowest lift coefficient of approximately $C_L = 0.31$. Furthermore, increasing the cavitation number to 0.91 reduced drag for all profiles by up to about 23%, while preserving lift in cambered foils. Pressure distribution and vapor volume fraction contours further support these observations, indicating stronger low-pressure regions on cambered foils. Time-resolved analyses revealed that cavitation structures grow and detach more rapidly at lower σ , especially for cambered geometries. These findings suggest that for applications where minimizing cavitation-induced performance degradation is critical, moderate camber with reduced thickness may offer a balance between lift generation and cavitation resistance. In high-lift-demand applications, cambered profiles may be preferred, while thicker symmetric sections could be more suitable for durability in high-load conditions despite their lower lift performance.

Author Contributions

The percentages of the author contributions are presented below. The author reviewed and approved the final version of the manuscript.

	M.N.K.	
C	100	
D	100	
S	100	
DCP	100	
DAI	100	
L	100	
W	100	
CR	100	
SR	100	
PM	100	
FA	100	

C=Concept, D= design, S= supervision, DCP= data collection and/or processing, DAI= data analysis and/or interpretation, L= literature search, W= writing, CR= critical review, SR= submission and revision, PM= project management, FA= funding acquisition.

Conflict of Interest

The author declared that there is no conflict of interest.

Ethical Consideration

Ethics committee approval was not required for this study because there was no study on animals or humans.

References

Adil S, Hussien HA, Othman SA. 2025. Detect cavitation in centrifugal hydraulic pumps: A Review. Iraqi J Oil Gas Res, 5(1): 1–19.

Arndt REA. 2012. Some remarks on hydrofoil cavitation. J Hydrodyn, 24(3): 305–314.

Canlı E, Ates A, Bilir Ş. 2020. Derivation of dimensionless governing equations for axisymmetric incompressible turbulent Flow Heat Transfer Based on Standard k- ϵ Model. Afyon Kocatepe Univ J Sci Eng, 20(6): 1096–1111.

Chen J, Escaler X. 2024. Numerical investigation of the cavitation effects on the wake dynamics behind a blunt trailing edge hydrofoil. Ocean Eng, 302: 117599.

Gallegos DP, Luo X. 2024. 3D study of cloud cavitation on a circular leading-edge hydrofoil using RANS approaches. ASME Fluids Eng Div Summer Conf Proc, pp:45-64.

Guo M, Liu C, Ke Z, Yan Q, Zuo Z, Khoo BC. 2023. Effects of flow conditions on the cavitation characteristics of viscous oil around a hydrofoil. Phys Fluids, 35: 1-15.

Huang B, Zhao Y, Wang G. 2014. Large Eddy Simulation of turbulent vortex-cavitation interactions in transient sheet/cloud cavitating flows. Comput Fluids, 92: 113-124.

Kang T, Park W, Jung C. 2014. Cavitation flow analysis of hydrofoil with change of angle of attack. J Comput Fluids Eng, 19: 17-23.

Karim M, Rahman M, Hai MA, Shimul MM, Sudhi SH. 2018. Numerical investigation of flow around cavitating hydrofoil using finite volume method. AIP Conf Proc, 1980: 40018.

Kaya MN, Satcunanathan S, Meinke M, Schröder W. 2025. Leading-edge noise mitigation on a rod-airfoil configuration using regular and irregular leading-edge serrations. Appl Sci, 15(14): 7822.

Kim SE, Schroeder S, Jasak H. 2010. A multi-phase CFD framework for predicting performance of marine propulsors. Proc 13th Int Symp Transport Phenomena Dyn Rotating Mach: 4–7.

Kubota A, Kato H, Yamaguchi H. 1992. A new modelling of cavitating flows: a numerical study of unsteady cavitation on a hydrofoil section. J Fluid Mech, 240: 59–96.

Kumar P, Sharma N, Pattanayek SK, Garg A. 2024. Computational comparison of passive control for cavitation suppression on cambered hydrofoils in sheet, cloud, and supercavitation regimes. Phys Fluids, 36: 1-18.

Manolesos M, Celik Y, Ramsay H, Karande R, Wood B, Dinwoodie I, Masters I, Harrold M, Papadakis G. 2024. Performance improvement of a Vestas V52 850kW wind turbine by retrofitting passive flow control devices. J Phys Conf Ser, 2767(2): 022027.

Mostafa N, Karim M, Sarker M. 2016. Numerical prediction of unsteady behavior of cavitating flow on hydrofoils using bubble dynamics cavitation model. J Appl Fluid Mech, 9: 1829-1837.

Peng XX, Ji B, Cao Y, Xu L, Zhang G, Luo X, Long X. 2016. Combined experimental observation and numerical simulation of the cloud cavitation with U-type flow structures on hydrofoils. Int I Multiph Flow. 79: 10-22.

Qiu Q, Gu Y, Ren Y, Mou C, Hu C, Ding H, Wu D, Wu Z, Mou J. 2025.

- Research progress in hydrofoil cavitation prediction and suppression methods. Phys Fluids, 37: 011301.
- Schnerr GH, Sauer J. 2001. Physical and numerical modeling of unsteady cavitation dynamics. Proc 4th Int Conf Multiph Flow, New Orleans, USA, pp: 1–12.
- Shen Y, Dimotakis P. 1989. Viscous and Nuclei Effects on Hydrodynamic Loadings and Cavitation of a NACA 66 (MOD) Foil Section. J Fluids Eng Trans ASME, 111: 306–316.
- Usta O, Öksüz S, Çelik F. 2025. Effect of leading-edge tubercles
- and surface corrugations on the performance and cavitation characteristics of twisted hydrofoils. Ocean Eng, 335: 121663.
- Wang F, Zhu B, Zhang W, Zhang H. 2025. Cylinder wake effect on cavitation flow field around a downstream hydrofoil. Phys Fluids, 37: 1-15.
- Zhou L, Wan Z. 2008. Numerical simulation of cavitation around a hydrofoil and evaluation of a RNG κ - ϵ model. J Fluids Eng Trans ASME, 130(1): 011302.